Pseudocapacitive Charge Storage in Thick Composite MoS_2 Nanocrystal Based Electrodes

John B. Cook,[1] Hyung-Seok Kim,[2] Terri C. Lin,[1] Chun-Han Lai,[2] Bruce Dunn,[2,3,*] Sarah H. Tolbert[1,2,3]*

[1]Department of Chemistry and Biochemistry, UCLA, Los Angeles, California 90095-1569, United States

[2]Department of Materials Science and Engineering, UCLA, Los Angeles, California 90095-1595, United States

[3]The California NanoSystems Institute, UCLA, Los Angeles, California 90095

[*]to whom correspondence should be addressed, tolbert@chem.ucla.edu, bdunn@ucla.edu

Keywords: *MoS_2, pseudocapacitance, intercalation-pseudocapacitance, li-ion battery, defected structure.*

Abstract:

In this work we demonstrate a synthesis methodology to produce MoS_2 nanoparticles with an expanded atomic lamellar structure that are ideal for Faradaic based capacitive charge storage. While much of the work on MoS_2 focuses on the high capacity conversion reaction of MoS_2, that process is prone to poor reversibility. In this study, we instead focus on pseudocapacitive intercalation based charge storage, which is extremely fast and highly reversible. A major challenge in the field of pseudocapacitive based energy storage is the development of thick electrodes from nanostructured materials that can sustain the fast inherent kinetics of the active nanocrystalline material. Here we utilize a composite electrode comprised of a poly(acrylic acid) binder and carbon fiber/carbon black additives. These electrodes deliver a specific capacity of 90 mAh/g in less than 20 seconds, and can be cycled 3000 times while retaining over 80% of the original capacity. Quantitative kinetic analysis indicates that over 80% of the charge storage in these MoS_2 nanocrystals is pseudocapacitive. Asymmetric full cell devices utilizing a MoS_2 nanocrystal based electrode and an activated carbon electrode achieve a maximum power density of 5.3 kW/kg (at 6 Wh/kg) and a maximum energy density of 37 Wh/kg (at 74 W/kg).

This is the author manuscript accepted for publication and has undergone full peer review but has not been through the copyediting, typesetting, pagination and proofreading process, which may lead to differences between this version and the Version of Record. Please cite this article as doi: 10.1002/smll.201601283.

1. Introduction

Fast charging batteries are highly desired for portable electronics, electric vehicles, and regenerative energy storage. Traditional Li-ion batteries offer high energy density storage by utilizing reversible redox reactions, but slow ionic diffusion leads to long charging times (~1 - 10 hours).[1] Electrochemical capacitors, such as electrochemical double layer capacitors (EDLCs), offer some advantages over batteries, including fast charging times (<1 minute) and long lifetimes (>500,000 cycles).[2] However, EDLCs have low energy densities (5-10 Wh/kg) compared to batteries (100-250 Wh/kg), since they do not involve redox reactions.[3]

Pseudocapacitors are another type of electrochemical capacitor that have the potential to combine the attractive high energy density storage of batteries with the fast rates of EDLCs.[4,5] Pseudocapacitance was originally described by Conway who identified faradaic mechanisms that can result in capacitive electrochemical features. The most useful of these for energy storage are redox pseudocapacitance and intercalation pseudocapacitance.[6,7] Redox pseudocapacitance occurs when a Faradaic charge transfer process take place at or near the surface of a material, accompanied by adsorption of charge balancing ions.[8–14] Conway originally described the pseudocapacitive mechanism to also include lithium intercalation into layered host materials,[6] but the majority of the work published in this field focuses on the surface redox-based electrochemical reactions of ultra-high surface area materials like RuO_2,[8–12] and MnO_2.[14] This bias toward materials showing surface pseudocapacitance has led to intercalation pseudocapacitance (another distinguishable pseudocapacitive mechanism) being dismissed or confused in some cases with traditional battery reactions. However, several papers clearly distinguish key differences between intercalation pseudocapacitance and battery-like reactions.[15–19] Intercalation pseudocapacitance is similar to familiar battery-type intercalation, but unlike traditional battery materials, the charge storage mechanism and electrochemical response is not dominated by diffusion limitations. Another key feature that distinguishes intercalation pseudocapacitance from traditional battery-type intercalation reactions is that these materials do not undergo phase transitions in association with charge storage.[18,19] As a result, materials that store charge dominantly through intercalation pseudocapacitance display fast kinetics and long cycle lifetimes.[17,18,20,21]

The electrochemistry of ruthenium oxide in acidic solutions exhibits classic surface redox pseudocapacitance, and has been studied for over 30 years because of its relatively high capacitances, high proton conductivity and high electronic conductivity. [8–10,12] However, the high cost of ruthenium has led groups to develop materials based on less expensive transition metals. We have developed a variety of oxide based nanostructures that store charge through intercalation pseudocapacitance, such as MoO_2,[18] MoO_3,[16,22] and Nb_2O_5.[17,22–24] As mentioned above, intercalation pseudocapacitance is distinguishable from diffusion dominated charge storage, and as a result, the characteristic electrochemical signatures are markedly different.[4,7,25] For example, the galvanostatic charge and discharge curves of pseudocapacitors are typically pseudo-linear with respect to intercalant concentration;

compared to batteries, which show plateaus.[26,27] Since intercalant diffusion does not dominate the charge storage in pseudocapacitors, the energy hysteresis between guest-ion insertion and deinsertion is typically small, which can be seen as a small peak separation in a cyclic voltammogram.[17,22–24] These properties lead to two key technologically relevant properties of pseudocapacitors: (1) The majority of the theoretical capacity can be accessed within minutes to seconds. (2) The reactions are highly reversible leading to low parasitic heat generation and long cycle lifetimes.

Much of the work on pseudocapacitors has focused on transition metal oxide based materials, but metal sulfides are attractive pseudocapacitive materials, too. The interaction between the guest ion (Li^+, for example), and the sulfide lattice, should be weakened compared to oxides. Furthermore, this weakened interaction should lead to faster ion migration through the lattice. In support of those ideas, we have recently demonstrated high levels of pseudocapacitive charge storage in TiS_2 nanoplatelets,[19] and mesoporous MoS_2 thin films.[21] MoS_2 is a particularly attractive pseudocapacitive electrode material because its large van der Waals gaps of 6.2 Å in micrometer sized samples increase up to 6.9 Å in nanostructured samples. [28,29] The increased van der Waals spacing should further reduce the guest-host interaction making this an ideal pseudocapacitive material.

MoS_2 also has a second advantage, which is that lithium insertion into the semi-conducting 2H phase of MoS_2 induces a phase transition to the metallic 1T phase of MoS_2.[30–33] This metallic phase is more conductive than the semi-conducting phase of MoS_2, which is an advantage for Faradaic based charge storage. The thermodynamically stable 2H phase of MoS_2 consists of sulfur atoms coordinated in a trigonal prismatic arrangement around the metal, while in the 1T phase, the atoms conform to an octahedral arrangement around the metal center.[34] The physical rearrangement of the molybdenum coordination environment induces a change in the electronic structure of the MoS_2, leading to metallic conductivity.[31] In agreement with this idea, our group has recently used conductive atomic force microscopy to demonstrate that ordered mesoporous 1T-MoS_2 thin films are significantly more conductive than the 2H form.[21] It was also recently reported that 10 nm thick exfoliated 1T-MoS_2 has a low sheet resistance (2 kΩ/sq),[35] corresponding to a calculated bulk conductivity of ~500 S/cm. In hydrogen evolution applications the intrinsically high electronic conductivity of 1T-MoS_2 is utilized to decrease the overpotential required for hydrogen evolution.[36] However, the high electronic conductivity of MoS_2 has not been fully leveraged in Li-ion battery applications because many studies have focused on high capacity conversion reaction of MoS_2, which interrupt the metallic 1T form of MoS_2. [29,37–46] Additionally, the volume change on cycling for the conversion reaction limits lifetimes to ~100-300 cycles. [47]

We note that Li^+ intercalation in MoS_2 is not a new idea. [48–50] MoS_2 was seriously considered as a commercial secondary battery in the 1980's because the reversibility is extremely favorable when the lithium concentration in MoS_2 is limited to 1 mole, [50–53] usually by limiting the lower cut-off voltage window to above 0.8 V vs. Li/Li^+.[54] In our previous paper, we demonstrated that mesoporous MoS_2 thin films exhibited high levels of

pseudocapacitive charge storage, emphasizing the promise of this material system as a fast charging, high power, long lifetime material.[21] That study motivated us to see if those observations were limited to thin films, or if those exciting properties could be recreated in thick film composite electrodes, as we have done here.

MoS_2 can be synthesized using a variety of different techniques. Monodispersed 5 nm MoS_2 nanocrystals can be synthesized directly by low temperature colloidal synthesis methods.[55] The hydrothermal method is another versatile technique, which has been used to synthesize a variety of nanostructured MoS_2 architectures.[29,56,57] However, both of these methods typically lead to very disordered crystal structures. The energy and power density of pseudocapacitive materials are, to a high degree, dependent on the crystallinity.[58] Therefore, in this work, we use a two-step process, first creating MoO_2 nanocrystals as a precursor using straightforward hydrothermal methods, and then converting those MoO_2 nanocrystals to MoS_2 nanocrystals. This two-step process enables precise control of both the nanoscale architecture and atomic-scale crystallinity. The synthesis method is versatile, and should be applicable to other nanoscale architectures such as wires, belts, and a broad range of porous architectures. Here we specifically use thermal sulfurization in H_2S to convert the MoO_2 to MoS_2, which preserves the carefully constructed nanoscale architecture formed from the solvothermal reaction.[44,56,59–61] This oxide-to-sulfide conversion is typically achieved above 600°C, which can lead to well crystalized MoS_2 with good preservation of the preformed nanoscale architecture.[56] It is worth noting that sulfur vapor can also be used instead of H_2S to convert molybdenum oxides to MoS_2.[62] Extensive discussion on the various methods used to synthesize MoS_2 can be found in several recent reviews.[47,63–65]

Commercial electrodes for Li-ion batteries are required to have high active material volumetric loadings to maximize the energy density of the cell. In order for this requirement to be satisfied in pseudocapacitive based composite electrodes, close attention also needs to be paid to the electrode architecture. The three main components that form a composite electrode are the active material, the conductive additive, and the non-conductive polymeric binder. Optimization of these parameters strongly influences the energy density and power density of the final electrode.[66,67] Furthermore, nanoparticle active material tends to agglomerate, making them difficult to disperse homogeneously within the electrode matrix.[68,69] This random agglomeration results in electronically resistive inter-particle contact, ultimately leading to poor power density due to inhomogeneous current gradients. Therefore, even if a material shows basic pseudocapacitive responses, the characteristic charge/discharge rates cannot be realized if the electrode architecture is not optimized for pseudocapacitive charge storage. Porous electrode architectures, which are highly electronically conductive, represents an effective design strategy to maintain the fast rates inherent to pseudocapacitive active materials.

In this study, we combine all of these ideas to synthesize MoS_2 nanocrystals with an expanded layer spacing for use as a high rate and long lifetime pseudocapacitor. The nanocrystals are fabricated into carbon fiber based composite electrode architectures, and the

electrodes show extremely fast charging and discharging kinetics along with long cycling lifetimes. We further utilize pre-cycling steps to convert the 2H phase into the highly conductive 1T phase, which then synergistically couples to the highly conductive carbon fiber mesh electrode architecture. Detailed electrochemical kinetic analyses performed on the nanocrystal based electrodes are used to quantify the amount of capacitive charge storage. These values can then be compared to electrodes containing micrometer size MoS_2 to fully establish advantages of the MoS_2 nanocrystal containing composite electrodes.

2. Results and Discussion

2.1 Materials and characterization

The MoS_2 nanocrystals (nc-MoS_2) studied in this report were synthesized by the sulfurization of hydrothermally prepared MoO_2 nanocrystals. The X-ray diffraction (XRD) patterns of bulk MoS_2 (b-MoS_2) and nc-MoS_2 match JCPDS No. 37-1492 (Figure 1a). We have refined the b-MoS_2 structure in Celref using the hexagonal P63/mmc hexagonal space group and aluminum foil as an internal standard. The lattice parameters for b-MoS_2 are $a \,\&\, b = 3.163\,\text{Å} \pm 0.002\,\text{Å}$ and $c = 12.3092\,\text{Å} \pm 0.0002\,\text{Å}$, which is in excellent

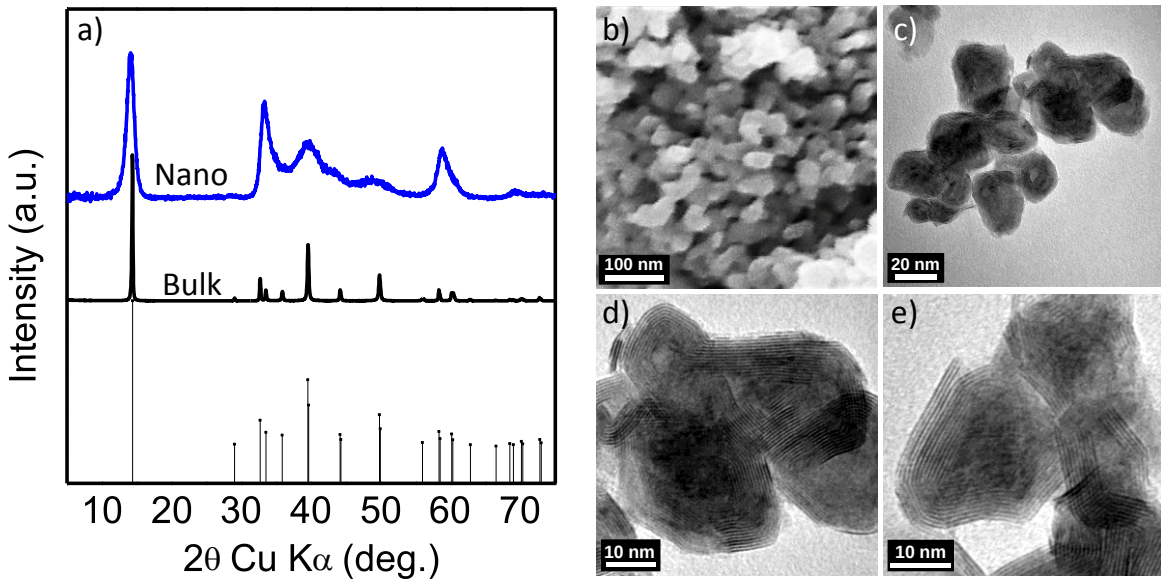

Figure 1. (a) X-ray diffraction of b-MoS_2 and nc-MoS_2 shows that both materials crystalize in the 2H hexagonal crystal structure (JCPDS 037-1492). The nc-MoS_2 shows significant peak broadening, however, which we assign to both finite size effects and lattice disorder. (b) Scanning electron microscope image of nc-MoS_2 show a network of agglomerated nanocrystals. (c-e) Transmission electron microscope images of dispersed nc-MoS_2 show sub-50 nanometer primary particles. Significant defects are observed and are believed to be at least partly responsible for the facile ion insertion into the bulk of the nanocrystal.

agreement with previously reported values for MoS_2.[70] The lattice parameters for nc-MoS_2 are $a \,\&\, b = 3.14\ Å \pm 0.01\ Å$ and $c = 12.544\ Å \pm 0.003\ Å$. The c-axis lattice parameter is expanded in the nanoparticles to 6.27Å, compared to 6.15Å for the bulk sample, in agreement with previous reports for nano-size MoS_2.[28,29] Furthermore, significant XRD peak broadening is observed for the nc-MoS_2 due to both finite size effects and lattice defects. The domain size calculated from the Scherrer equation is 7 nm, which is smaller than the primary particle size observed from the scanning electron microscopy (SEM) and transmission electron microscopy images (TEM) in Figure 1b and 1c, respectively. This difference in the calculated Scherrer size versus observed size clearly indicates that the XRD peak broadening is due to a combination of finite size effects and lattice disorder. In agreement with this idea, defects and curvature of the MoS_2 layers can be clearly seen in the high resolution TEM images (Figures 1d and e).

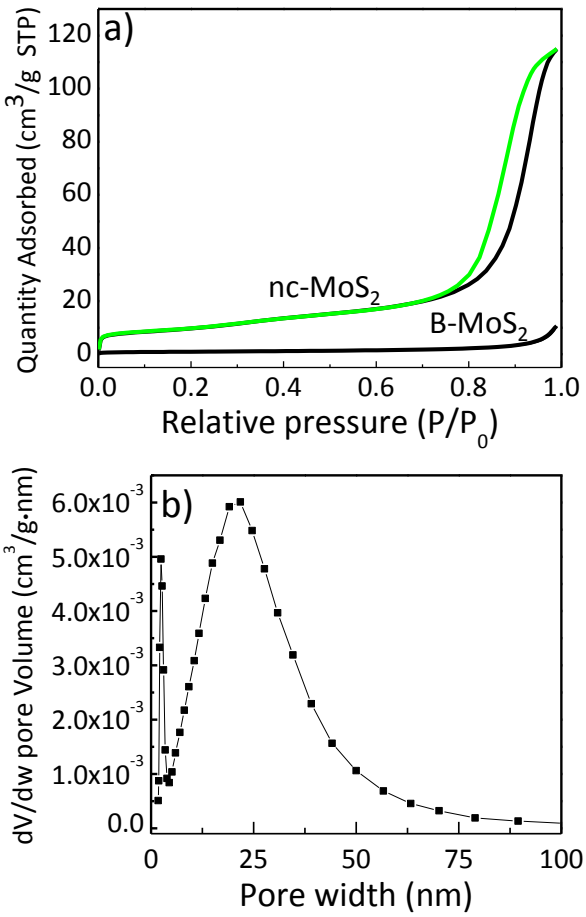

Figure 2. Nitrogen isotherm of both b-MoS_2 and nc-MoS_2 (a). The calculated surface area for nc-MoS_2 is 35m^2g^{-1} while the bulk is 2 m^2g^{-1}. This 17.5-fold increase in surface area, in part, leads to the pseudocapacitive charge storage mechanism. BJH pore size distribution calculated from the adsorption isotherm in part (a) for nc-MoS_2 (b). The porosity shown in the BJH distribution arises from adhesion of the nanocrystals to each other, which creates pores.

Beyond the primary particle size and lattice structure, Figure 1b further shows that in bulk form, the nanocrystals aggregated into a nearly ideal interconnected porous network. The surface area and pore sizes in that network can be characterized using nitrogen porosimetry. The surface area for both b-MoS_2 (2 m^2/g) and nc-MoS_2 (35 m^2/g) was calculated from the nitrogen adsorption isotherms shown in Figure 2a using the Brunauer-Emmett-Teller (BET) method.[71] The surface area of the nc-MoS_2 is almost twenty-times larger than b-MoS_2, and leads to a higher density of redox active surface sites for pseudocapacitive charge storage. This is coupled to short intra-grain diffusion distance, which favor intercalation-pseudocapacitance. The pore size distribution shown in Figure 2b

was calculated using the Barrett-Joyner-Halenda (BJH) method,[72] and was used to characterize the pores that are created in the nc-MoS_2 by adhesion of the nanocrystals to each other. The pore size distribution is remarkably narrow for a material formed by random nanocrystal agglomeration, and the 25 nm pore diameter is well suited to allow facile electrolyte diffusion into the nanoparticle aggregates.

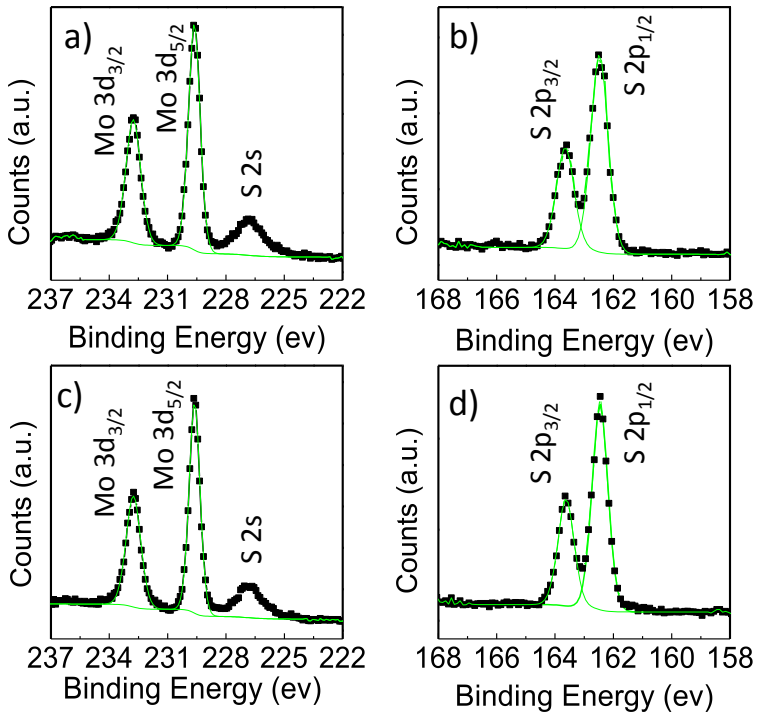

Figure 3. X-ray photoelectron spectroscopy of b-MoS_2 (a, b) and nc-MoS_2 (c, d). The data can be well fit with a single 4+ oxidation state for Mo and a 2- oxidation state for S. The elemental stoichiometry calculated from the data is 1.05:2.00, Mo:S. These data thus show that the surface of the nc-MoS_2 is the same as the commercial bulk powder, and both surfaces are consistent with bulk MoS_2.

The chemical surface properties of b-MoS_2 and nc-MoS_2 were examined using X-ray photoelectron spectroscopy (XPS), as shown in Figure 3. These high resolution spectra can be fit with a single oxidation state for both Mo and S, corresponding to the Mo^{4+} and S^{2-} valence states. The peak area ratio between these two elements further yield a Mo:S = 1.05:2.00 stoichiometry ratio for both samples. Since the surface chemistry is identical in bulk and nano-sized samples, strong conclusions can be drawn about the effect of size, surface area, and atomic disorder on the enhanced electrochemical performance in the nano-sized materials.

2.2 Electrochemistry

The reversible lithium insertion and deinsertion process for MoS_2 is represented by the following equation:

$$MoS_2 + xLi^+ + xe^- \leftrightarrow Li_xMoS_2 \qquad \text{where: } 0 \leq x \leq 1 \qquad \text{Equation 1}$$

Intercalation of Li-ions proceeds through the weakly bonded van der Waals gaps of MoS_2.[47,73] The lithium ion binding energy is higher for adsorption into the octahedral interstitials compared to the tetrahedral interstitials, and hence is preferentially stored in the octahedral sites between sulfur layers.[74] Below $x = 0.1$ in Li_xMoS_2 intercalation into the 2H-MoS_2 occurs without much change to the initial atomic lattice structure.[57] However,

increasing the concentration of Li between the range $0.1 < x < 1$ causes an advantageous irreversible phase change from the semiconducting 2H phase to the metallic 1T phase at ca. 1.0 V *vs.* Li/Li^+.[31,75] This phase change does not involve a significant structural rearrangement, but instead is accomplished by a glide process of the highly polarizable sulfur layers with respect to the molybdenum plane.[76]

Figure 4 shows dQ/dV plots of the first ten formation cycles at 1C of b-MoS_2 and nc-MoS_2 (carbon fiber based electrodes). The 2H-to-1T phase transition is observed electrochemically as the large differential charge response at ca. 1.2 V *vs.* Li/Li^+ in Figures 4a and c. Figures 4b and d show the same data with cycle 1 omitted (cycles 2 – 10), so that the evolution of lower intensity peaks can be more easily observed. The data clearly demonstrate the nc-MoS_2 electrodes require multiple cycles to convert to the 1T phase while b-MoS_2 is rapidly converted just after 2 cycles. This type of behavior is often seen in nanocrystal based phase transitions where many isolated nucleation events are needed to fully transform a sample.[77] During the ten formation cycles at 1C, new cathodic and anodic peaks develop, and correspond to the lithiation / delithiation of the electronically conductive MoS_2 1T phase.[78] Raman spectroscopy was also performed on lithiated nc-MoS_2 to verify the formation of the 1T MoS_2 phase (Figure SI-1). The results show the development of four additional peaks between 120-350 cm^{-1}, which can be assigned to the 1T phase of MoS_2; along with the loss of the 2H E_{1g} peak at 281 cm^{-1}.[21,36,79,80] All other peaks in the Raman spectra are shared by both the 2H and 1T phases. The combination of both electrochemical and spectroscopic characterization provides strong evidence that nc-MoS_2 is converted to the 1T phase during these first ten cycles.

Electrochemical impedance spectroscopy was then used to characterize changes in conductivity as a function of pre-cycling. Figure 4e shows the charge transfer resistance of both nc-MoS_2 and b-MoS_2, which was obtained from their respective Nyquist plots (Figure SI-2a and c). The equivalent circuit model used to fit our data, and representative fits using that model, is shown in Figure SI-2d, f, and g. This model fits our data well, and has been used to fit the impedance spectra of hydrous RuO_2, another pseudocapacitive material.[10] During the formation cycles (0.8 V – 3.0 V *vs.* Li/Li^+), the charge transfer resistance is reduced by the 2H-to-1T phase change, and increased by the formation of the solid electrolyte interphase (SEI). The net result for both nc-MoS_2 and b-MoS_2 is that the charge transfer resistance increases during the first two cycles, mainly due to SEI formation, followed by a gradual decay during the next eight cycles mainly due to the formation of the

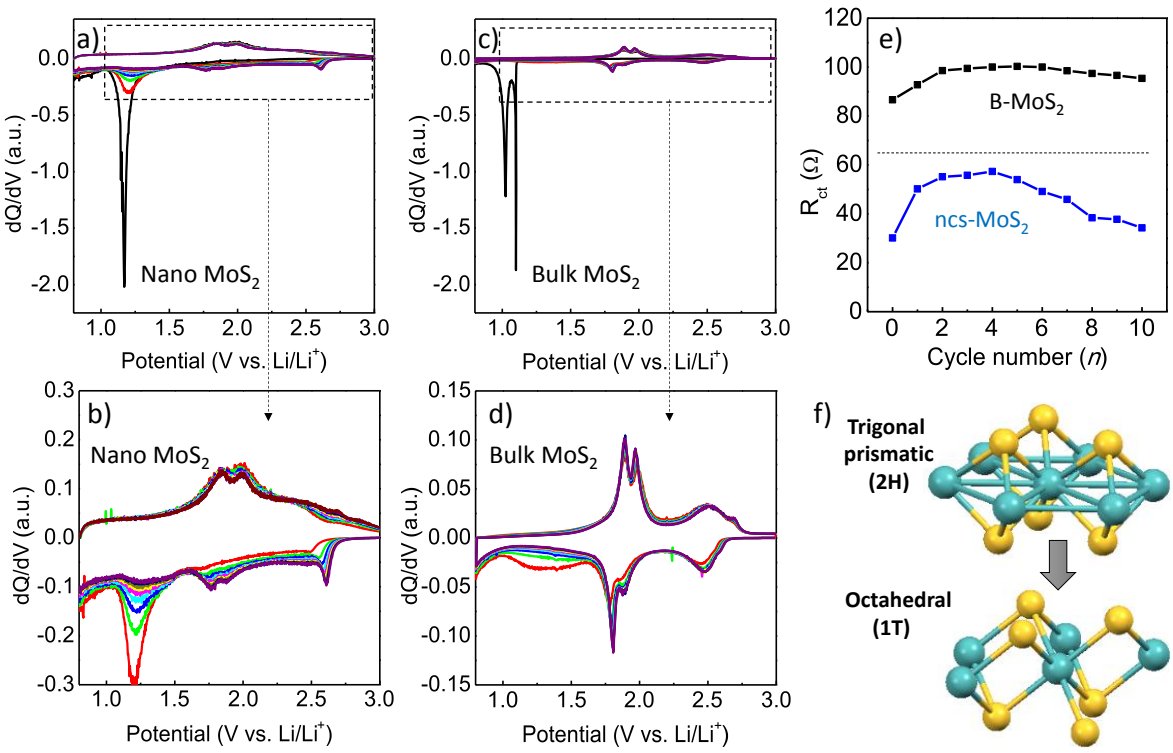

Figure 4. Derivative of the galvanostatic charge discharge plot dQ/dV of the first 10 cycles of nc-MoS_2 (a), and b-MoS_2 (c) showing the irreversible phase transition and subsequent formation of the highly electronically conducting 1T-MoS_2 phase. dQ/dV of cycles 2 - 9 of nc-MoS_2 (b), and b-MoS_2 (d) which shows that the 2H –to – 1T phase change occurs over 10 cycles, while in b-MoS_2 the phase change has occurred after the second cycle. Charge transfer resistance of b-MoS_2 and nc-MoS_2 based electrodes during the first 10 formation cycles calculated from the corresponding Nyquist plots. Impedance collected at 3V vs. Li/Li^+ (green), and 0.8 V vs. Li/Li^+ (black) (e). Atomic representation of the 2H-to-1T phase transformation. This transformation only involves a small shift in the easily polarized sulfur layer, which is non-destructive to the nanoscale structure (f).

electronically conductive 1T phase.

Electrode architectures for high rate pseudocapacitive charge storage were optimized in order to maximize the properties of the electronically conductive MoS_2 1T phase. One effective way to achieve highly conductive and porous composite electrodes, is to utilize carbon fibers. The shape anisotropy of the carbon fibers can lead to a highly porous mesh that extends from the current collector throughout the electrode.[81,82] In this work, the electrode components are sonicated together in ethanol to disperse the nanocrystals homogeneously with the carbon fibers and carbon black, which upon drying lead to a highly conductive and porous electrode. We chose to use a poly(acrylic acid) binder since it has demonstrated high rate performance in other systems.[83,84] SEM images of these electrodes are shown in Figure 5c and SI-3a, which demonstrate that the carbon fiber based electrodes consist of a mesh-type network that appears to be macroporous. A traditional electrode formulation of polyvinylidene fluoride binder and carbon black was used as a comparative baseline to understand the synergy between the electrode architecture, composition, and the

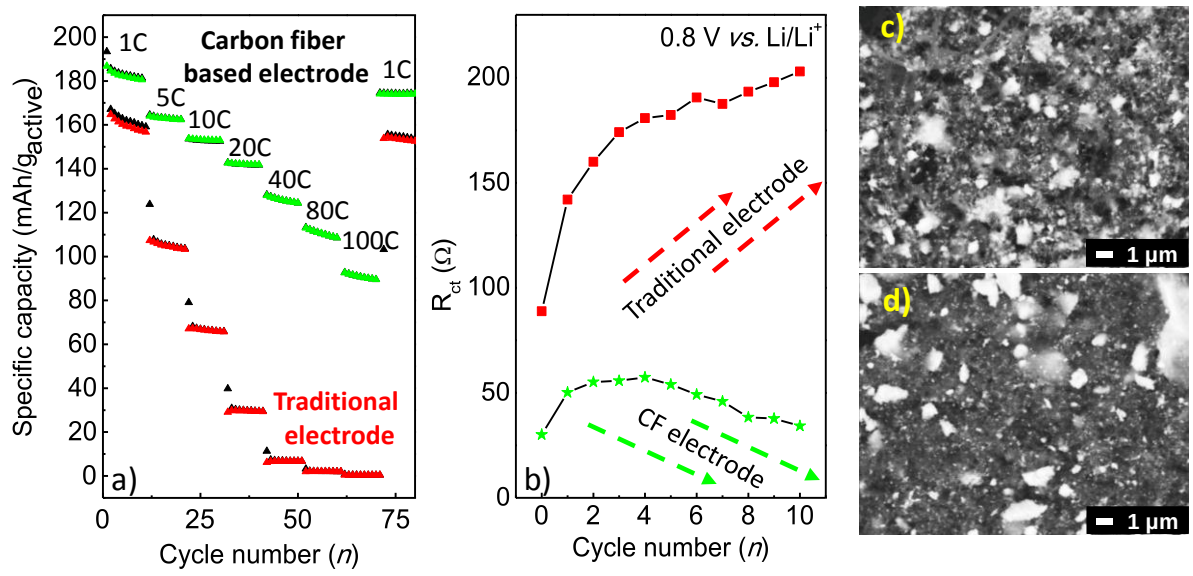

Figure 5. (a) Galvanostatic kinetic analysis, after 10 formation cycles, comparing nc-MoS_2 electrodes made using carbon fibers and mixed using sonication (green), and electrodes made using only carbon black and mixed using a traditional mortar and pestle (red). (b) Charge transfer resistance of nc-MoS_2 / carbon fiber based electrodes (green), and nc-MoS_2 / carbon black based electrodes (red) during the first 10 formation cycles calculated from Nyquist plots collected at 0.8 V vs. Li/Li^+. The charge transfer in the carbon fiber based electrode is both lower in absolute value, and decreases with cycle number because the newly formed 1T MoS_2 is electronically well connected to the electrode architecture. By contrast, the charge transfer resistance in the traditional carbon black based electrodes monotonically increases, likely due to SEI formation. Backscatter electron images of the carbon fiber based electrode (c) and carbon black only electrode (d). The brightness in backscattered images is related to the atomic Z number, so the dark-regions are carbon rich and the light-regions are MoS_2 rich.

pseudocapacitive active material (Figures 5d and SI-3b). In Figures SI-3c and d we also present cartoons of the traditional carbon black electrodes and the carbon fiber based electrodes.

The kinetic performance of nc-MoS_2 is shown for these two different electrode formulations in Figure 5a. The nc-MoS_2 active material in the carbon fiber based electrodes show much better kinetic performance compared to the traditional electrodes. We believe that both particle dispersion and electronic conductivity are dominating factors leading to the superior performance. The traditional electrodes were mixed by hand with mortar and pestle, and the final composite electrode probably suffers from poor nanoparticle dispersion since nanoparticles tend to agglomerate. In contrast, the carbon fiber based electrodes were mixed using sonication and show extremely good kinetic performance. Sonication assisted mixing homogeneously distributes the nanocrystals throughout the electrode, [85] enabling synergistic coupling between the nc-MoS_2 1T-conductive phase and the conductive carbon scaffold. It has previously been shown that improving dispersion in nanocrystal based electrodes can produce markedly better rate performance compared to traditional electrodes.[68]

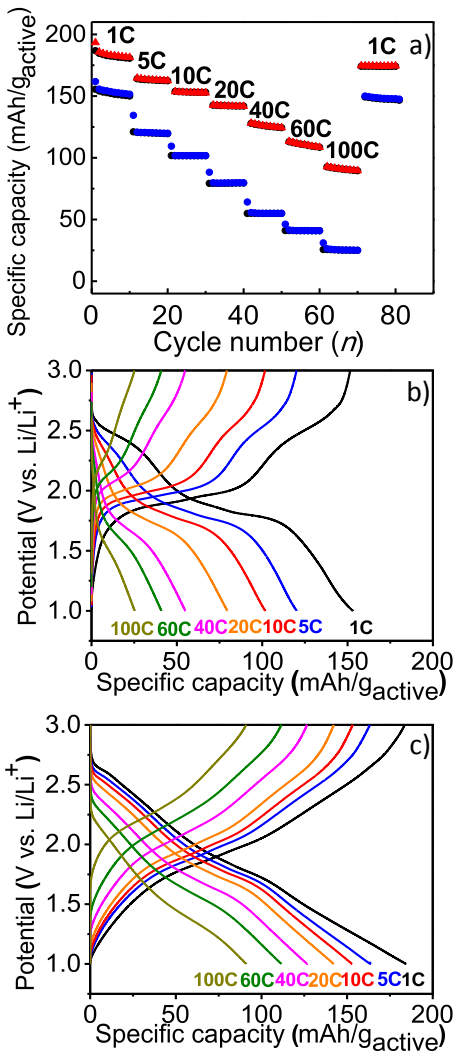

Figure **6.** (a) Galvanostatic kinetic analysis comparing b-MoS_2 to the nc-MoS_2 in optimized carbon fiber based electrodes (a). The nanostructured material stores nearly four-times the charge at 100C compared to b-MoS_2. Galvanostatic lithium insertion and deinsertion profiles at different current densities of b-MoS_2 (b), and nc-MoS_2 (c). The galvanostatic traces for the nc-MoS_2 based electrodes are pseudo-linear and are quite different from the standard plateaus observed for b-MoS_2.

In order to further understand the disparity in kinetics between the two different electrode formulations, we also performed electrochemical impedance spectroscopy on the carbon black based nc-MoS_2 electrodes. The Nyquist plots are shown in Figures SI-2b and e, and the same equivalent circuit model mentioned previously was also used to fit this data. We found that the pristine charge transfer resistance is significantly higher in the carbon black based electrode architecture compared to the carbon fiber based electrode architecture. Furthermore, the charge transfer resistance of the carbon black based electrodes increase over the first ten formation cycles in stark contrast

to the decrease in charge transfer resistance of the carbon fiber based electrodes over the same interval (Figures 5b and SI-2). This data suggests that the improved rate kinetics in the carbon fiber based electrodes are a combination of the dispersed nanocrystals in the composite electrode, and the good electronic coupling of the nanocrystals to the carbon scaffolding.

Using the optimized carbon fiber based electrode architecture enables the quantification of important metrics related to pseudocapacitors in a standard slurry-type electrode. We can now move on to compare these metrics between b-MoS_2 and nc-MoS_2 fabricated in the same electrode architecture to understand how nanostructuring affects the electrochemical properties. The kinetic analysis of the nc-MoS_2 shown in Figure 6 shows markedly better rate performance compared to b-MoS_2. The nc-MoS_2 electrodes retain 50% of the original 1C capacity at 100C while the b-MoS_2 electrodes retain only 17%. Remarkably, these thicker film electrodes based on nc-MoS_2 store more than 90 mAh/g in less than 20 seconds.

We calculated the RC time constants for the three electrode systems developed in this work to better understand the nature of the fast kinetic response (see experimental section). After ten cycles between 0.8 – 3.0 V *vs.* Li/Li^+ the RC time constant for the non-optimized carbon black based electrode with nc-MoS_2 active material is 2.74 ms. In contrast the RC time constants of b-MoS_2 and nc-MoS_2, in optimized carbon fiber based electrodes, are 1.86 ms and 1.26 ms, respectively. The optimized electrode architecture decreases the RC time constant two-fold for nc-MoS_2. The synergistic coupling of the metallic nanocrystals and the conductive carbon fiber backbone like produces a low electrode resistance that is responsible for the enhancement in the RC time constant. These RC time constant values are fairly short

Material type	Guest ion	Slow rate A/g, mAh/g	Fast rate A/g, mAh/g	Capacity retention cycles, % retention	Reference
nc-MoS_2	Li^+	**0.167, 182**	**16.7, 91**	**3000, 81**	**this study**
Hydrothermal MoS_2	Li^+	0.2, 200	3, 50	1400, 83*	[48]
Fullerene type MoS_2	Na^+	0.1, 160	4, 61	30, 47	[50]
Exfoliated MoS_2 (thin film)	H^+	5 mV/s, 57** (potentiostatic)	100 mV/s, 49** (potentiostatic)	5000, 75	[94]

Table 1. Gravimetric capacity of nanostructured MoS_2 based half-cells. *The capacity increased from ~200 – 220 mAh/g over ~500 cycles, so we normalized the capacity retention by the maximum capacity value and not the initial capacity of 200 mAh/g. **The capacitance reported in this study was converted to capacity using the reported voltage window of 0.85V. The galvanostatic trace used to calculate the capacitance are nearly linear, so the relationship capacity = (capacitance · Voltage)/3.6 is an excellent approximation for this system.

compared to other pseudocapacitive materials, likely as a result of the metallic nature of the active material.[86]

In order to compare these exciting performance results discussed above to other state of the art MoS_2 based pseudocapacitors, we have aggregated important performance characteristics of non-conversion type reactions (including both intercalation and surface reactions) in (Table 1). At low current densities, the nc-MoS_2 reported here delivers similar capacity to the best materials reported to date. Most materials reported in the table show current densities between 3-4 A/g as their fastest rates, and the nc-MoS_2 reported here delivers 142 mAh/g at a current density of 3.3 A/g, a value two to three-fold higher than other materials included in the table. Even when nc-MoS_2 is cycled at 16.7 A/g, the delivered capacity is still nearly double the capacities reported for the other materials at a significantly lower current density. In our recent work on nanostructured MoS_2 thin films, we found similarly fast kinetics,[21] but what makes this report significant, is the ability to preserve those rates in thicker composite electrodes. This is enabled through the porous electrode morphology and coupling of the highly conductive 1T-MoS_2 nanocrystals to the composite electrode architecture.

The fast charge transfer kinetics in nc-MoS_2 can also be understood by the physical charge storage mechanism of ions in the material. Figure 6b shows the galvanostatic charge and discharge traces for b-MoS_2 between 1C and 100C. These traces display the traditional stepped plateau features that are indicative of charge storage accompanied by a phase transition in a battery material. Structural studies have shown that indeed bulk 1T Li_xMoS_2 undergoes multiple first order phase changes during Li-ion storage.[78] Phase transformations are in part responsible for the sluggish kinetics in battery-type materials because the nucleation and propagation of new phases are typically slow. In contrast to b-MoS_2, Figure 6c shows galvanostatic traces for nc-MoS_2 that display a pseudo-linear voltage response with respect to Li-ion concentration. This sloping response is a hallmark of pseudocapacitance, and is also indicative of a solid-solution storage mechanism where no phase change occurs to accommodate the lithiation.[18,19] As described in the introduction, pseudocapacitance occurs whenever the charge (Q) depends on the change in potential (dE), yielding a capacitance (dQ=dE).[3] Although these charge storage redox processes are Faradaic in nature, their phenomenological behavior, and response to experimental variables such as sweep rate, are those typical of capacitors. Generally, the dependency of the current response on the sweep rate in a cyclic voltammetry experiment can be utilized to distinguish the charge storage process according to Equation 2. [87,88]

$$i = av^b \qquad \text{Equation 2}$$

In the framework of this analysis, the measured current i is fit to a power law with scan rate v, and the exponential term b can be determined from the slope of the *log* (i) *vs. log* (v) plot. Values of b = 0.5 indicate that the current is proportional to the square root of the scan rate, which is consistent with traditional diffusion dominated charge storage.[87] On the other hand,

when b = 1 the current is linearly proportional to the scan rate, which is characteristic of a capacitor-like charge storage mechanism.[87] Figure 7 shows several of the cyclic voltammograms used to calculate the b-values at the current maxima in the anodic and cathodic regimes. The b-values that are calculated for b-MoS_2 are labeled on the CV plots next to the corresponding peaks used in their calculation. The various peaks display values between 0.65 – 0.83. These values are indicative of a diffusion dominated charge storage mechanism, as expected for micrometer size MoS_2. The b-values for nc-MoS_2 samples are generally much higher, and are found to be between 0.93-1.00, indicating that the dominant charge storage mechanism in the nanocrystal based electrodes is capacitor-like. The fast rate performance in nc-MoS_2 is enabled by this capacitive-type charge storage mechanism, quantified using Equation 2.

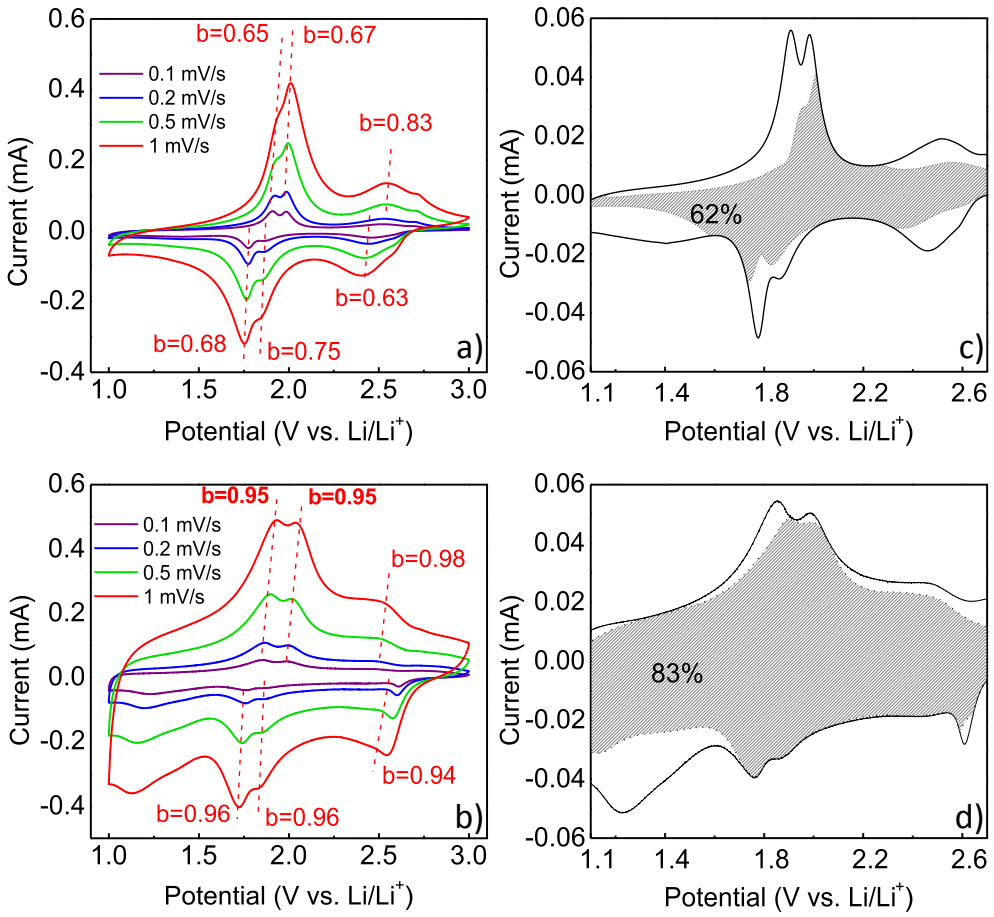

Figure 7. Analysis of the charge storage in the current maxima for b-MoS_2 (a) and nc-MoS_2 (b) using b-values calculated from Equation 2. This analysis shows that the Faradaic charge storage associated with the peak maxima in CV has a significant diffusion contribution in b-MoS_2, while this analysis shows that the same Faradaic processes are capacitive-like in nc-MoS_2. Quantification of the capacitive and diffusion charge storage in b-MoS_2 (c) and nc-MoS_2 (d) as a function of voltage. This analysis indicates that the nc-MoS_2 based electrodes store charge largely through a capacitive mechanism.

Another related analysis using cyclic voltammetry enables the measured current (i) at a fixed potential (V) to be quantitatively separated into a diffusion contribution and a capacitive contribution.[89]

$$i(V) = k_1 v + k_2 v^{0.5} \qquad \text{Equation 3}$$

In Equation 3, $k_1 v$, and $k_2 v^{0.5}$ correspond to capacitive and diffusion contributions to the measured current, respectively, where v is the scan rate in mV/s. Equation 3 enables the capacitive charge storage at specific potentials to be quantified along with total capacitive contribution over the entire voltage range. Figure 7 shows the results of this analysis for b-MoS_2, and indicates that charge storage is largely diffusion controlled at current maxima in

the cyclic voltammograms, which is supported by the calculated peak current b-values calculated from Equation 2. The total integrated capacitive charge storage is about 60%, which indicates that the parent atomic structure of MoS_2 is an extremely good candidate for pseudocapacitive charge storage.

When we perform the same analysis on nc-MoS_2, we find that over 80% of the charge storage is capacitive in nature. Furthermore, the capacitive current is significantly enhanced at the peak maxima voltages compared to b-MoS_2, again in good agreement with the calculated b-values from Equation 2, which are close to 1 in all cases. The broad non-capacitive cathodic peak in Figure 7d ca. 1.6 – 1.1 V *vs.* Li/Li^+ is attributed to the 2H-to-1T phase transformation. Even though this phase transition was largely completed before running these CV scans, some slow CV scan rates were used for this analysis to compare the slower diffusion processes in b-MoS_2 to the fast storage processes in nc-MoS_2. However, it has been reported that the 1T MoS_2 phase can convert back to the 2H phase at higher voltages,[78] and this is apparently occurs in the nc-MoS_2 samples cycled at the slowest rates (see Figure SI-4). As indicated in Figure 7d, the 2H-to-1T phase transition in the nc-MoS_2 is largely diffusion limited. We expect that even higher total capacitive contributions are possible by elimination of this phase transition by limiting the time that the nc-MoS_2 electrode spends in the fully delithiated state (3.0 V).

The origin of this fast capacitive charge storage mechanism in nc-MoS_2 can be described through structural considerations. Much of the structural information available on the electrochemical phase stability of MoS_2 has focused on the so called 2H (semiconductor with hexagonal symmetry) to 1T (metal with trigonal symmetry) transformation.[31,32,36,75,90] Once this conversion is complete, the 1T-metallic MoS_2 phase has been reported to undergo several first-order phase transformations[78] between 1 – 2.8 V *vs.* Li/Li^+; therefore, the fast kinetics observed here raises a fundamental question about the underlying charge storage processes occurring with nc-MoS_2 because these phase transitions should be slow. We have shown in both an oxide and sulfide based material system that phase transformation suppression is a hallmark of pseudocapacitive charge storage.[18,19] We thus postulate that similar effects are also occurring here. If charge storage kinetics are not limited by the nucleation and propagation of new phases, charge storage can proceeded directly through fast migration of ions through the weakly interacting sulfide lattice. The sloping voltage profiles observed in the galvanostatic measurements in Figure 7 for nc-MoS_2 electrodes strongly

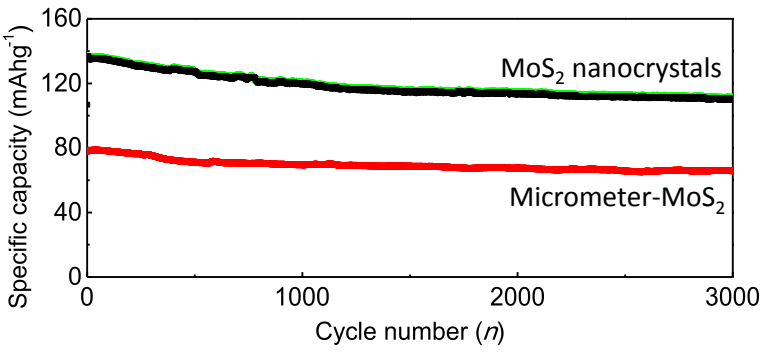

Figure 8. Cycle lifetime of nc-MoS_2 and b-MoS_2 electrodes cycled at 20C. Cycle 1 reported here was started after the kinetic study (1C-100C) shown in Figure 7. The long cycle lifetime and high capacity of the nc-MoS_2 is correlated with the established pseudocapacitive charge storage mechanism.

suggests that phase transitions are being suppressed here.

High levels of capacitive charge storage are often associated with long cycle life, and this system is no exception. The cycling stability measured for b-MoS_2 and nc-MoS_2 is shown in Figure 8, and indicates capacity retention for both samples is above 80% after 3000 cycles at 20C. The excellent cycling performance of the b-MoS_2 and nc-MoS_2 is mainly attributed to small structural changes (after the initial formation of the 1T phase) with a reported expansion in the c-axis direction of only ~ 4-6%.[57] The charge storage capacity in nc-MoS_2 at 20C is nearly 70% greater after 3000 cycles compared to b-MoS_2 as a result of its superior charge transfer properties. Referring back to Table 1, the nc-MoS_2 composite electrodes also cycle more reversibly than all of the intercalation based entries in the table as a result of the pseudocapacitive charge storage mechanism.

While the half-cell experiments described above provide a clear picture of fundamental redox processes occurring in these MoS_2 based electrodes, they do not fully demonstrate the potential of these materials in practical devices. To this end, a final set of experiments were performed to assess the technological relevance of this new pseudocapacitive electrode. Hybrid lithium capacitor devices were fabricated using an activated carbon cathode and a nc-MoS_2 anode. Activated carbon (AC) is a typical electrochemical capacitor material used in EDLCs for high rate applications, but the energy density is low compared to Faradaic storage processes because charge is stored only in the double layer of the electrode-electrolyte interface.[2,3] Figure 9a shows the hybrid lithium capacitor device made from a nc-MoS_2 and AC electrode delivers 37 Wh/kg at slow rates. In comparison, symmetric AC devices cycled in a similar electrolyte, and between a similar voltage window, delivers a maximum energy of ~20 Wh/kg.[91] The redox based charge storage mechanism found in the nc-MoS_2 is responsible for producing a higher energy density than the double layer charge storage of AC based devices. If an appropriate pseudocapacitive cathode was used instead of the AC, even higher energy density would be expected. The

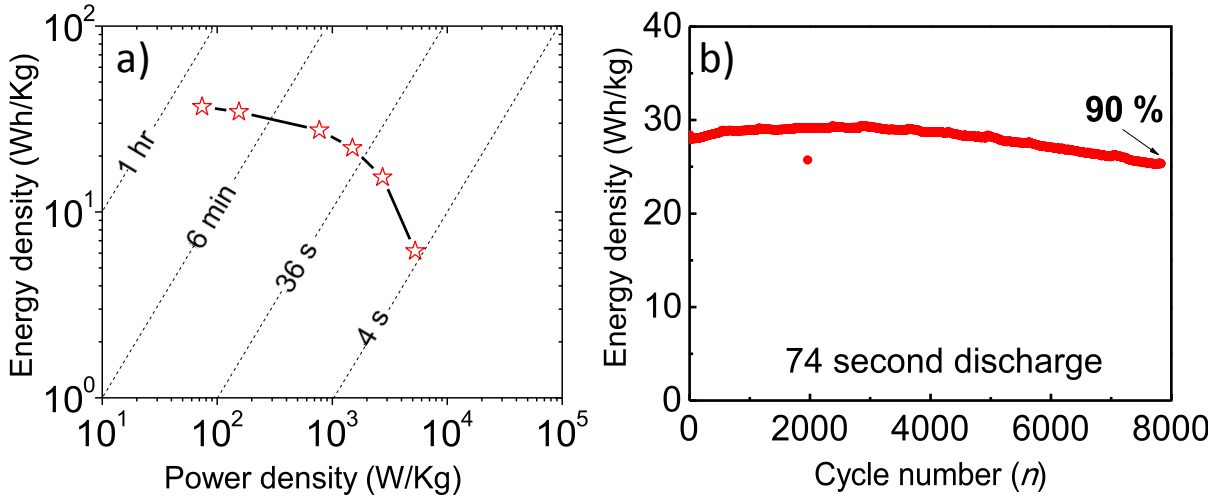

Figure 9. Average discharge energy density *vs.* average discharge power density for a full cell utilizing a nc-MoS_2 anode and an activated carbon cathode. The voltage of this device operates between 0.4 – 3.2 V. Average discharge energy density *vs.* cycle number for an asymmetric nc-MoS_2 / activated carbon full cell. (b) The voltage of this device operates between 0 – 3.0 V. The fast kinetics and long lifetime is a result of the highly reversible pseudocapacitive charge storage mechanism. This data was mass normalized using the total active mass of both electrodes (~4 mg).

maximum power density of the nc-MoS_2 hybrid devices is 5.3 kW/kg (6 Wh/kg), while symmetric AC devices in similar conditions are reported to only deliver 3.5 kW/kg (2 Wh/kg).[91] Furthermore, the energy densities and power densities of this sulfide based material are comparable with the other state of the art oxide hybrid lithium-ion capacitors, such as Nb_2O_5-AC,[91] TiO_2-AC,[92] and $Li_4Ti_5O_{12}$-AC[93] chemistry. Figure 9b further shows the excellent reversibility of the nc-MoS_2 full cell, which can be cycled 8,000 times with little decay in the delivered energy. This data thus indicates that nc-MoS_2 full cells overlap with the power density typically thought to be limited to double-layer type EC devices, while also overlapping with the energy density of some Li-battery materials.

3. Conclusions:

We have successfully synthesized high surface area MoS_2 nanocrystals with expanded van der Waals gaps, which show high levels of pseudocapacitive charge storage when built into a composite electrode. We have also demonstrated that the electrode architecture can be a dominating factor in the development of composite electrodes in pseudocapacitors. The high capacitive contribution measured for the nc-MoS_2 based electrodes is due to the interplay between the nanoscale architecture of the active material and the composite electrode. The high surface area and expanded layer structure of nc-MoS_2 enable fast Faradaic reactions, which leads to charge storage that appears capacitive even though ion migration occurs over distances that normally would be limited by semi-infinite diffusion. We have shown that over 80% of the charge storage is capacitive in nanocrystal based electrodes, which enables over 90 mAh/g to be accessed in only 20 seconds. Furthermore, the cycling stability of nc-MoS_2 shows over 80% retention after 3000 cycles as a result of the pseudocapacitive charge storage mechanism. Full cell devices utilizing an activated carbon cathode and an nc-MoS_2 anode show extremely attractive charge storage behavior and little capacity fade after 8000 cycles. Moreover, the energy density of devices based on nc-MoS_2 could be almost doubled if a cathode with similar kinetic performance is developed.

The results of this study highlight the importance of sulfide based pseudocapacitive active charge storage materials. The large 2-D galleries of MoS_2 and other metal chalcogenides make them of particular interest to the pseudocapacitive charge storage field. The next frontier will be developing new sulfide materials that enable intercalation pseudocapacitance over large length scales. This work also highlights the dire need for composite electrode architectures that are optimized for nanostructured pseudocapacitive active materials. The electrodes discussed in this work represent a significant accomplishment, but if practical devices are to be made from pseudocapacitive materials like these, attention needs to be paid to the synergistic coupling of the active material and the composite electrode in order to move to even thicker composite electrodes. We hope this demonstration of attractive electrochemical properties in sulfide based pseudocapacitors will stimulate the exploration of other chalcogenide based materials.

4. Experimental:

4.1 Synthesis

All starting materials were obtained from commercial suppliers and used without further purification. The synthesis of nanosized-MoO_2 has been reported elsewhere,[18] and is briefly described here. MoO_2 nanocrystals were prepared solvothermally by dissolving anhydrous $MoCl_5$ (Strem Chemicals) in a mixture of ethanol and deionized water at a reaction temperature of 180°C for 6 hrs. The MoO_2 nanocrystals were converted to MoS_2 with H_2S gas. The reaction was carried out in a tube furnace at 600°C under flowing H_2S/H_2 (H_2S 5 mol % : H_2 95 mol %, Air Gas) for 10 hours. A graphite boat was used to convert ~ 100 - 200 mg of MoO_2 to MoS_2.

Characterization

Powder X-ray diffraction (XRD) was performed in a PANalytical X'Pert Pro operating with Cu Kα (λ = 1.5418 Å) using a 0.03° step size, a voltage of 45kV, and a current of 40mA. XRD patterns were recorded in the range of $10° < 2\theta < 80°$. Transmission electron microscopy (TEM) was performed using an FEI Technai T12 operating at 120 kV. Nitrogen porosimetry was carried out using a Micromeritics TriStar II 3020. The surface area was calculated from the adsorption branch of the isotherm between (0.04 – 0.30 P/Po) using the Brunauer-Emmett-Teller (BET) model. The pore diameter and pore volume was also calculated from the adsorption branch of the isotherm using the Barret-Joyner-Halenda (BJH) model. X-ray photoelectron spectroscopy (XPS) analysis was performed using a Kratos Axis Ultra DLD with a monochromatic Al (Kα) radiation source. The charge neutralizer filament was used to control charging of the sample, 20 eV pass energy was used with a 0.1 eV step size, and scans were calibrated using the C 1s peak shifted to 284.8 eV. The integrated area of the peaks was found using the CasaXPS software, and atomic ratios were also found using this software. The atomic sensitivity factors used were from the Kratos library within the Casa software.

Raman spectroscopy was performed using a Renishaw inVia Raman confocal microscope (excitation wavelength 514 nm and 200 mW laser power) to study the 2H – 1T phase change in bulk and nano MoS_2. Raman spectroscopy was performed on pristine and lithiated (0.8V) state of both bulk and nano MoS_2 on the 11^{th} cycle to ensure the majority of the 2H phase is converted to 1T phase. Raman samples were cycled on Arbin at 1C from 0.8V -3.0V as half cells in swageloc cells using lithium metal as counter electrode, glass fiber (Watman) as separator, and 1M $LiPF_6$ in a 1:1 ethylene carbonate/ diethylene carbonate solvent (Sigma) as electrolyte.

4.2 Electrochemistry

The carbon fiber based electrodes were made from a slurry consisting of 70 wt.% nc-MoS_2 or b-MoS_2 (Alfa Asear) powder used as the active component for Li storage, 10 wt.% vapor grown carbon fibers (Sigma Aldrich), 10 wt.% carbon black (Alfa Asear) used as conductive additive, and 10 wt.% polyacrylic acid solution (M_w=250K, Sigma Aldrich) used as binder. The polyacrylic acid was used as a predissolved 5 wt.% solution in 200 proof ethanol. A typical slurry was prepared with 40 mg nc-MoS_2, 5.7 mg carbon black, 5.7 mg carbon fiber, 114 mg 5 wt.% polyacrylic acid solution, and 1 ml 200 proof ethanol. These four components were sonicated for 30 minutes to obtain a homogeneous dispersion. Ethanol evaporation over one hour resulted in a homogeneous thick paste that was cast onto 25 µm carbon coated Al foil (gift from Coveris) using doctor blading. The slurry was dried at ambient temperature for 1 h, and further dried at 25°C under vacuum overnight to evaporate the excess solvent. The traditional electrode was made from a slurry consisting of 70 wt.% nc-MoS_2, 20 wt.% carbon black (Alfa Asear), and 10 wt.% polyvinyl difluoride (gift from Kynar) dissolved in n-methyl-2-pyrrolidone (Alfa Asear). Components were mixed using a mortar and pestle, and again cast onto 25 µm carbon coated Al foil using doctor blading. The electrodes were dried in a vacuum oven at 110°C overnight. The mass loading of all the electrodes in this study were ~1 mg/cm^2 of active material. These electrodes were assembled into in-house built SwageLoc cells using lithium metal as counter electrode, glass fiber (Watman) as separator, and 1 M $LiPF_6$ in a 1:1 ethylene carbonate/dimethylcarbonate solvent (Sigma Aldrich) with 5% (v/v) fluorinated ethylene carbonate (TCI America) as electrolyte. Half-cell cycling was carried out on a VSP potentiostat/galvanostat (Bio-Logic) using a 1C rate that corresponds to 167 mAh/g. The half cells were precycled ten times between 0.8 - 3.0 V *vs.* Li/Li^+ to drive the 2H-1T phase transition before the kinetic analysis and cycling stability measurements.

4.3 Full cells

SwageLoc cells were used to cycle the full cells. Those devices were made with a nc-MoS_2 anode and an activated carbon cathode in a 1:5 active material ratio, respectively. The activated carbon electrodes were fabricated from YP50F activated carbon (85 wt%), carbon nanotubes (CNTs) (5 wt%), and polyvinylidene fluoride (PVDF) (10 wt%). These components were mixed in n-methyl-2-pyrrolidone (Alfa Asear) to form a homogeneous slurry, and cast onto a stainless steel sheet by doctor blading. The cast electrode sheet was dried in vacuum at 110°C for 12 hours. The electrodes were removed from the substrate to form free-standing electrodes with mass loadings of 4 - 6 mg/cm^2. As with the half cells described above, the nc-MoS_2 electrodes in all full cells were precycled ten times between 0.8 - 3.0 V *vs.* Li/Li^+ to drive the 2H-1T phase transition before the full cell device testing. The same electrolyte used in the half-cell testing was used for the full cell testing. The active mass of both electrodes was used to calculate the energy density and power density.

4.4 Electrochemical impedance spectroscopy

Electrochemical impedance spectroscopy was carried out on a VSP potentiostat/galvanostat (Bio-Logic). The impedance measurements were performed on two-electrode SwageLoc cells between 900 kHz and 100 mHz using a 10 mV input under no bias. Impedance data was collected at 0.8V *vs.* Li/Li^+ after each insertion cycle. A 5 minute potentiostatic hold was applied before each impedance measurement during which time the current dropped from ~200 mA/g to ~20 mA/g. The impedance spectra was fit using the Z fit plug-in available in EC-Lab V10.40 (Bio-Logic). RC time constants were calculated at 0.8V after ten cycles between 0.8 – 3.0 V. These values were derived from the frequency at the maximum imaginary resistance of the semi-circle in the Nyquist representation. At this point, $\omega = 1/RC$.

Acknowledgements:

This work was supported by the US Department of Energy, Office of Science, Basic Energy Sciences under Award Number DE-SC0014213 (ST). This funding was used principally for materials synthesis, structural characterization, and electrochemical measurements. Additional support for this research was also provided by the Office of Naval Research (BD, additional electrochemical measurements).

5. References

[1] B. Scrosati, *J. Echem. Soc.* **1992**, *139*, 2776.

[2] M. Winter, R. J. Brodd, *Chem. Rev.* **2004**, *104*, 4245.

[3] P. Simon, Y. Gogotsi, *Nat. Mater.* **2008**, *7*, 845.

[4] P. Simon, Y. Gogotsi, B. Dunn, *Science* **2014**, *343*, 1210.

[5] V. Augustyn, P. Simon, B. Dunn, *Energy Environ. Sci.* **2014**, *7*, 1597.

[6] B. E. Conway, V. Birss, J. Wojtowicz, *J. Power Sources* **1997**, *66*, 1.

[7] B. E. Conway, *J. Electrochem. Soc.* **1991**, *138*, 1539.

[8] N. Yoshida, Y. Yamada, S. I. Nishimura, Y. Oba, M. Ohnuma, A. Yamada, *J. Phys. Chem. C.* **2013**, *117*, 12003.

[9] J. P. Zheng, *J. Electrochem. Soc.* **1995**, *142*, L6.

[10] W. Wang, S. Guo, I. Lee, K. Ahmed, J. Zhong, Z. Favors, F. Zaera, M. Ozkan, C. S. Ozkan, *Sci. Rep.* **2014**, *4*, 4452.

[11] D. Michell, D. A. J. Rand, R. Woods, *J. Electroanal. Chem.* **1978**, *89*, 11.

[12] J. P. Zheng, P. J. Cygan, T. R. Jow, *J. Echem. Soc.* **1995**, *142*, 2699.

[13] Z. Tong, Y. Yang, J. Wang, J. Zhao, B.-L. Su, Y. Li, *J. Mater. Chem. A* **2014**, *2*, 4642.

[14] L. Deng, G. Zhu, J. Wang, L. Kang, Z. H. Liu, Z. Yang, Z. Wang, *J. Power Sources* **2011**, *196*, 10782.

[15] A. A. Lubimtsev, P. R. C. Kent, B. G. Sumpter, P. Ganesh, *J. Mater. Chem. A* **2013**, *1*, 14951.

[16] T. Brezesinski, J. Wang, S. H. Tolbert, B. Dunn, *Nat. Mater.* **2010**, *9*, 146.

[17] V. Augustyn, J. Come, M. A. Lowe, J. W. Kim, P. Taberna, S. H. Tolbert, H. D. Abruña, P. Simon, B. Dunn, *Nat. Mater.* **2013**, *12*, 1.

[18] H.-S. Kim, J. B. Cook, S. H. Tolbert, B. Dunn, *J. Electrochem. Soc.* **2015**, *162*, A5083.

[19] G. A. Muller, J. B. Cook, H.-S. Kim, S. H. Tolbert, B. Dunn, *Nano Lett.* **2015**, *15*, 1911.

[20] Z. Chen, V. Augustyn, J. Wen, Y. Zhang, M. Shen, B. Dunn, Y. Lu, *Adv. Mater.* **2011**, *23*, 791.

[21] J. B. Cook, H.-S. Kim, Y. Yan, J. S. Ko, S. Robbennolt, B. Dunn, S. H. Tolbert, *Adv. Energy Mater.* **2016**, *6*, 1501937.

[22] K. Brezesinski, J. Wang, J. Haetge, C. Reitz, S. O. Steinmueller, S. H. Tolbert, B. M. Smarsly, B. Dunn, T. Brezesinski, *J. Am. Chem. Soc.* **2010**, *132*, 6982.

[23] V. Augustyn, J. Come, M. A. Lowe, J. W. Kim, P. Taberna, S. H. Tolbert, H. D. Abruña, P. Simon, B. Dunn, *Nat. Mater.* **2013**, *12*, 1.

[24] K. Brezesinski, J. Wang, J. Haetge, C. Reitz, S. O. Steinmueller, S. H. Tolbert, B. M. Smarsly, B. Dunn, T. Brezesinski, *J. Am. Chem. Soc.* **2010**, *132*, 6982.

[25] A. G. Dylla, G. Henkelman, K. J. Stevenson, *Acc. Chem. Res.* **2013**, *46*, 1104.

[26] E. Lim, H. Kim, C. Jo, J. Chun, K. Ku, S. Kim, H. Lee, I.-S. Nam, S. Yoon, K. Kang, J. Lee, *ACS Nano* **2014**, *8*, 8968.

[27] M. Okubo, E. Hosono, J. Kim, M. Enomoto, N. Kojima, T. Kudo, H. Zhou, I. Honma, *J. Am. Chem. Soc.* **2007**, *129*, 7444.

[28] Y. Liang, R. Feng, S. Yang, H. Ma, J. Liang, J. Chen, *Adv. Mater.* **2011**, *23*, 640.

[29] H. Hwang, H. Kim, J. Cho, *Nano Lett.* **2011**, *11*, 4826.

[30] F. Wypych, R. Schollhorn, *J. Chem. Soc., Chem. Commun.* **1992**, 1386.

[31] M. A. Py, R. R. Haering, *Can. J. Phys.* **1983**, *61*, 76.

[32] Y.-C. Lin, D. O. Dumcenco, Y.-S. Huang, K. Suenaga, *Nat. Nanotechnol.* **2014**, *9*, 391.

[33] L. F. Mattheiss, *Phys. Rev. B* **1973**, *8*, 3719.

[34] E. Benavente, M. A. S. Ana, F. Mendiza, G. Gonza, *Coord. Chem. Rev.* **2002**, *224*, 87.

[35] F. Xiong, H. Wang, X. Liu, J. Sun, M. Brongersma, E. Pop, Y. Cui, *Nano Lett.* **2015**, *15*, 6777.

[36] H. Wang, Z. Lu, S. Xu, D. Kong, J. J. Cha, G. Zheng, P.-C. Hsu, K. Yan, D. Bradshaw, F. B. Prinz, Y. Cui, *Proc. Natl. Acad. Sci. U. S. A.* **2013**, *110*, 19701.

[37] H. Li, K. Yu, H. Fu, B. Guo, X. Lei, Z. Zhu, *J. Phys. Chem. C.* **2015**, *119*, 7959.

[38] L. David, R. Bhandavat, U. Barrera, G. Singh, *Sci. Rep.* **2015**, *5*, 9792.

[39] A. P. Tiwari, H. Yoo, J. Lee, D. Kim, J. H. Park, H. Lee, *Nanoscale* **2015**, *7*, 11928.

[40] F. Sun, Y. Wei, J. Chen, D. Long, L. Ling, Y. Li, J. Shi, *Nanoscale* **2015**, *7*, 13043.

[41] J.-Z. Wang, L. Lu, M. Lotya, J. N. Coleman, S.-L. Chou, H.-K. Liu, A. I. Minett, J. Chen, *Adv. Energy Mater.* **2013**, *3*, 798.

[42] S. H. Choi, Y. N. Ko, J.-K. Lee, Y. C. Kang, *Adv. Funct. Mater.* **2015**, *25*, 1780.

[43] G. Du, Z. Guo, S. Wang, R. Zeng, Z. Chen, H. Liu, *Chem. Commun.* **2010**, *46*, 1106.

[44] H. Liu, D. Su, R. Zhou, B. Sun, G. Wang, S. Z. Qiao, *Adv. Energy Mater.* **2012**, *2*, 970.

[45] H. Jiang, D. Ren, H. Wang, Y. Hu, S. Guo, H. Yuan, P. Hu, L. Zhang, C. Li, *Adv. Mater.* **2015**, *27*, 3687.

[46] F. Xiong, Z. Cai, L. Qu, P. Zhang, Z. Yuan, O. K. Asare, W. Xu, C. Lin, L. Mai, *ACS Appl. Mater. Interfaces* **2015**, *7*, 12625.

[47] T. Stephenson, Z. Li, B. Olsen, D. Mitlin, *Energy Environ. Sci.* **2014**, *7*, 209.

[48] Z. Hu, Q. Liu, W. Sun, W. Li, Z. Tao, S. Chou, J. Chen, S. X. Dou, *Inorg. Chem. Front.* **2016**, *3*, 532.

[49] C. Julien, S. I. Saikh, G. A. Nazri, *Mater. Sci. Eng. B.* **1992**, *15*, 73.

[50] S. H. Woo, L. Yadgarov, R. Rosentsveig, Y. Park, D. Song, R. Tenne, S. Y. Hong, *Isr. J. Chem.* **2015**, *55*, 599.

[51] D. Ilic, K. Wiesener, W. Schneider, G. Krabbes, H. Oppermann, *J. Power Sources* **1985**, *14*, 223.

[52] A. J. Jacobson, R. R. Chianelli, M. S. Whittingham, *J. Electrochem. Soc.* **1979**, 34.

[53] J. J. Auborn, *J. Electrochem. Soc.* **1987**, *134*, 580.

[54] R. R. Haering, J. A. Stiles, K. Brandt, *(Moli Energy Ltd) US Patent*, **1980**.

[55] H. Yu, Y. Liu, S. L. Brock, *Inorg. Chem.* **2008**, *47*, 1428.

[56] X. Fang, X. Yu, S. Liao, Y. Shi, Y.-S. Hu, Z. Wang, G. D. Stucky, L. Chen, *Microporous Mesoporous Mater.* **2012**, *151*, 418.

[57] T. Stephenson, Z. Li, B. Olsen, D. Mitlin, *Energy Environ. Sci.* **2014**, *7*, 209.

[58] T. Brezesinski, J. Wang, S. H. Tolbert, B. Dunn, *Nat. Mater.* **2010**, *9*, 146.

[59] X. W. Lou, H. C. Zeng, *Chem. Mater.* **2002**, *14*, 4781.

[60] H. C. Zeng, F. Xie, K. C. Wong, K. a. R. Mitchell, *Chem. Mater.* **2002**, *14*, 1788.

[61] J. A. Arnoldy, P;van den heijkant, J. A. M.; de Bok, G. D; Moulijn, *J. Catal.* **1985**, *55*, 35.

[62] M. V Reddy, R. Jose, A. Le Viet, K. I. Ozoemena, B. V. R. Chowdari, S. Ramakrishna, *Electrochim. Acta* **2014**, *128*, 198.

[63] X. Hu, W. Zhang, X. Liu, Y. Mei, Y. Huang, *Chem. Soc. Rev.* **2015**, *44*, 2376.

[64] Q. Lu, J. G. Chen, J. Q. Xiao, *Angew. Chem. Int. Ed. Engl.* **2013**, *52*, 1882.

[65] Y. Zhao, Y. Zhang, Z. Yang, Y. Yan, K. Sun, *Sci. Technol. Adv. Mater.* **2013**, *14*, 043501.

[66] G. Liu, H. Zheng, A. S. Simens, A. M. Minor, X. Song, V. S. Battaglia, *J. Electrochem. Soc.* **2007**, *154*, A1129.

[67] A. Ponrouch, M. R. Palacín, *J. Power Sources* **2012**, *212*, 233.

[68] T. J. Patey, A. Hintennach, F. La Mantia, P. Novák, *J. Power Sources* **2009**, *189*, 590.

[69] C. Jiang, M. Ichihara, I. Honma, H. Zhou, *Electrochim. Acta* **2007**, *52*, 6470.

[70] R. G. Dickinson, L. Pauling, *J. Am. Chem. Soc.* **1923**, *45*, 1466.

[71] S. Brunauer, L. S. Deming, W. E. Deming, E. Teller, *J. Am. Chem. Soc.* **1940**, *1139*, 1723.

[72] E. P. Barrett, L. G. Joyner, P. P. Halenda, **1951**, *73*, 373.

[73] Y. Jung, Y. Zhou, J. Cha, *Inorg. Chem. Front.* **2016**, *3*, 452.

[74] Y. Li, D. Wu, Z. Zhou, C. R. Cabrera, Z. Chen, *J. Phys. Chem. Lett.* **2012**, *3*, 2221.

[75] X. Fang, C. Hua, X. Guo, Y. Hu, Z. Wang, X. Gao, F. Wu, J. Wang, L. Chen, *Electrochim. Acta* **2012**, *81*, 155.

[76] M. A. Py, R. R. Haering, *Can. J. Phys.* **1983**, *61*, 76.

[77] S. H. Tolbert, A. P. Alivisatos, *Science.* **1994**, *265*, 373.

[78] P. J. Mulhern, *Can. J. Phys.* **1989**, *67*, 1049.

[79] S. Jiménez-Sandoval, D. Yang, R. Frindt, J. Irwin, *Phys. Rev. B* **1991**, *44*, 3955.

[80] M. A. Lukowski, A. S. Daniel, F. Meng, A. Forticaux, L. Li, S. Jin, *J. Am. Chem. Soc.* **2013**, *135*, 10274.

[81] V. Sivasankaran, C. Marino, M. Chamas, P. Soudan, D. Guyomard, J. C. Jumas, P. E. Lippens, L. Monconduit, B. Lestriez, *J. Mater. Chem.* **2011**, *21*, 5076.

[82] B. Lestriez, S. Desaever, J. Danet, P. Moreau, D. Plée, D. Guyomard, *Electrochem. Solid-State Lett.* **2009**, *12*, A76.

[83] C. Erk, T. Brezesinski, H. Sommer, R. Schneider, J. Janek, *ACS Appl. Mater. Interfaces* **2013**, *5*, 7299.

[84] N. P. W. Pieczonka, V. Borgel, B. Ziv, N. Leifer, V. Dargel, D. Aurbach, J. H. Kim, Z. Liu, X. Huang, S. A. Krachkovskiy, G. R. Goward, I. Halalay, B. R. Powell, A. Manthiram, *Adv. Energy Mater.* **2015**, *5*, 1501008.

[85] A. Ponrouch, M. R. Palacín, *J. Power Sources* **2011**, *196*, 9682.

[86] K. Makgopa, P. M. Ejikeme, C. J. Jafta, K. Raju, M. Zeiger, V. Presser, K. I. Ozoemena, *J. Mater. Chem. A* **2015**, *3*, 3480.

[87] J. Wang, J. Polleux, J. Lim, B. Dunn, *J. Phys. Chem. C* **2007**, *111*, 14925.

[88] H. Lindström, S. Södergren, A. Solbrand, H. Rensmo, J. Hjelm, A. Hagfeldt, S.-E. Lindquist, *J. Phys. Chem. B* **1997**, *101*, 7717.

[89] T.-C. Liu, *J. Electrochem. Soc.* **1998**, *145*, 1882.

[90] N. Imanishi, M. Toyoda, Y. Takeda, O. Yamamoto, *Solid State Ionics* **1992**, *58*, 333.

[91] V. Augustyn, W. Kim, P. Rozier, P. Taberna, P. Gogotsi, J. W. Long, B. Dunn, P. Simon, *J. Echem. Soc.* **2014**, *161*, 718.

[92] H. Kim, M. Y. Cho, M. H. Kim, K. Y. Park, H. Gwon, Y. Lee, K. C. Roh, K. Kang, *Adv. Energy Mater.* **2013**, *3*, 1500.

[93] H. G. Jung, N. Venugopal, B. Scrosati, Y. K. Sun, *J. Power Sources* **2013**, *221*, 266.

[94] Q. Mahmood, S. K. Park, K. D. Kwon, S. J. Chang, J. Y. Hong, G. Shen, Y. M. Jung, T. J. Park, S. W. Khang, W. S. Kim, J. Kong, H. S. Park, *Adv. Energy Mater.* **2016**, *6*, 1.

Table of contents entry

MoS_2 nanocrystals were synthesized by the thermal sulfurization of hydrothermally prepared MoO_2 nanocrystals. Composite electrodes were formulated to show high levels of pseudocapacitive charge storage in traditional slurry based systems. These electrodes can be charged and discharged to 50% of theoretical capacity in just 20 seconds, and can be reversibly cycled 3,000 times with greater than 80% capacity retention.